

UC Merced

UC Merced Previously Published Works

Title

Diffuse optical tomography for breast cancer imaging guided by computed tomography: A feasibility study

Permalink

<https://escholarship.org/uc/item/7t02s7m7>

Journal

Journal of X-Ray Science and Technology, Preprint(Preprint)

ISSN

0895-3996

Authors

Baikejiang, Reheman
Zhang, Wei
Li, Changqing

Publication Date

2017

DOI

10.3233/xst-16183

Peer reviewed

Diffuse optical tomography for breast cancer imaging guided by computed tomography: a feasibility study

Reheman Baikejiang^a, Wei Zhang^a, Changqing Li^{a,*}

^a School of Engineering, University of California, Merced, 5200 N. Lake Road, Merced, CA, USA, 95343

Abstract. Diffuse optical tomography (DOT) has attracted attentions in the last two decades due to its intrinsic sensitivity in imaging chromophores of tissues such as hemoglobin, water, and lipid. However, DOT has not been clinically accepted yet due to its low spatial resolution caused by strong optical scattering in tissues. Structural guidance provided by an anatomical imaging modality enhances the DOT imaging substantially. Here, we propose a computed tomography (CT) guided multispectral DOT imaging system for breast cancer imaging. To validate its feasibility, we have built a prototype DOT imaging system which consists of a laser at the wavelength of 650 nm and an electron multiplying charge coupled device (EMCCD) camera. We have validated the CT guided DOT reconstruction algorithms with numerical simulations and phantom experiments, in which different imaging setup parameters, such as projection number of measurements and width of measurement patch, have been investigated. Our results indicate that an air-cooling EMCCD camera is good enough for the transmission mode DOT imaging. We have also found that measurements at six angular projections are sufficient for DOT to reconstruct the optical targets with 2 and 4 times absorption contrast when the CT guidance is applied. Finally, we have described our future research plan on integration of a multispectral DOT imaging system into a breast CT scanner.

Keywords: Diffuse optical tomography, multi-modality imaging, breast cancer imaging

* Changqing Li, cli32@ucmerced.edu, (209) 228-4777

1. INTRODUCTION

In the United States of America, breast cancer ranks second in all cancers in terms of cancer mortality in female population.¹ Breast cancer screening, especially if being capable of early detection, is one of the efficient approaches to reduce the mortality rate caused by breast cancer.² Mammography has been used widely for breast cancer screening, but it is difficult to diagnose breast cancers for breasts with high mammographic density and/or micro-calcifications.³ Ultrasound imaging has higher sensitivity than mammography in imaging dense breast but with low specificity in screening breast cancers.^{4,5} Magnetic resonance imaging (MRI) was reported to have results correlated better with pathology findings than mammography and obtained promising results when dynamic contrast agents are applied.⁶⁻⁸ However, MRI is expensive and exogenous agents are needed for better contrast. In 1990s, diffuse optical tomography (DOT) has emerged with promises as an imaging tool for breast cancer screening and diagnosis because of its unique features such as non-ionizing radiation, low cost, and high intrinsic absorption contrast.⁹

We use continuous wave (CW) measurement data due to its simplicity and low cost. CW measurements at multiple wavelengths in the near infrared (NIR) wavelength range were used to reconstruct different absorption chromophores in tissues.¹⁰⁻¹⁴ Most DOT breast imaging systems used fibers to deliver lasers to breast surface and collected the diffused light on the breast surface, in which the measurement number was determined by the optode pairings.^{11,15-22} To increase the number of measurement data, Culver *et al.* reported a charge coupled device (CCD) camera based DOT imaging system.²³ Turner *et al.* used a CCD camera to measure early photons in a DOT imaging system.²⁴ In this study, we used an electron multiplying CCD (EMCCD) camera to measure light intensity on the breast surface in a transmission mode.

DOT is an ill-conditioned inverse problem and suffers low spatial resolution. To enhance the DOT reconstruction, anatomical priors were introduced.²⁵⁻³⁰ Fang *et al.* reported a Tomosynthesis/3D-mammogram guided DOT imaging system.^{31,32} Brooksby *et al.* and Ntziachristos *et al.* reported MRI guided, fiber based DOT imaging systems.^{33,35} Zhu and colleagues used ultrasound imaging to guide the DOT imaging.^{18,36} These studies have shown substantial improvements in quality and accuracy of DOT imaging with structural priors. However, these systems have limitations. Tomosynthesis is not a true three-dimensional (3D) imaging modality thus its structural guidance is not sufficient. And the imaged breast is compressed during the tomosynthesis/3D-mammogram scan which might cause discomfort to patients. For MRI guidance, MRI is very expensive and the patients with some metal implants cannot be imaged by MRI. For ultrasound imaging guidance, approximations are required for coregistering the two-dimensional (2D) ultrasound images to the 3D optical measurements.³⁶ Our proposed CT guided DOT imaging system will not have these limitations.

In this paper, we report a novel CT guided DOT system for breast cancer imaging. The spatial resolution of the DOT system is improved with the anatomical guidance obtained from CT imaging. There are several advantages of this proposed system. Firstly, although breast CT system uses X-ray photons, the radiation dose is less than or equivalent to that of a two-projection mammography, which is minimal.^{37,38} Secondly, because we use an EMCCD camera to acquire optical measurement data, our system is non-contact, does not need coupling fluid, and will not bring any pain or discomfort during the scanning. Lastly, with the use of an EMCCD camera, we can have abundant measurement data for DOT reconstruction, although the camera may have limited sensitivity of measurements.

The rest of this article is organized as follows. In section 2, we introduce methods and materials. Then we report the results from numerical simulations and phantom experiments. Finally, we end the paper with discussion and future work.

2. METHODS AND MATERIALS

2.1 DOT prototype system

The DOT prototype system built in our lab consisted of an EMCCD camera (C9100-13, Hamamatsu) with a lens (Schneider Xenon 25mm f/ 0.95), a diode laser at 650 nm with a collimator (BWF-OEM-650-200-100-0.22, B&W Tek, Inc), a linear stage (XN10-0060-E01-71, Velmex, Bloodfield, NY) and a rotary stage (B4872TS-ZRS, Velmex, Bloomfield, NY). As shown in Fig. 1, the imaged phantom was placed on the rotation stage. The EMCCED camera was mounted on its right side with a distance of 25 cm to the phantom boundary so that the field of view (FOV) of the camera covered the whole phantom. The laser collimator was mounted on a linear stage and was 1 cm away from the phantom surface on the left side. A laser beam was collimated to have a diameter less than 2 mm on the phantom surface. During the experiments, the EMCCD camera stayed stationary while the rotary stage rotated the phantom with an angular step of 60 degrees. For each rotary angle, the linear stage moved the collimated laser beam 6 steps in the vertical direction with a step size of 5 mm. For one set of measurements, there were 36 laser illumination points on the phantom of interest. For each illumination position, three images were taken by the EMCCD camera and averaged to reduce measurement noises.

2.2 Forward model and reconstruction algorithm of DOT

The propagation of light in turbid media such as biological tissues can be modeled precisely by the radiative transfer equation (RTE).³⁹⁻⁴² Because it is difficult to solve the RTE, the diffusion

equation is widely accepted as an approximation to the RTE in DOT imaging. The finite element method (FEM) is used to solve the diffusion equation.^{42,43} And due to the ill-posed nature of the inverse problem in DOT, regularization methods are used to stabilize the DOT reconstruction.^{44,45}

2.2.1 Forward modeling

In the CW domain, NIR light propagation in turbid media is modeled by the diffusion equation,⁴⁶ which is given as

$$-\nabla \cdot [\kappa(r)\nabla\Phi(r)] + \mu_a(r)\Phi(r) = Q_0(r), \quad (1)$$

where ∇ denotes the gradient operator, $\Phi(r)$ and $Q_0(r)$ are the photon density and the isotropic light source at position r , respectively, and $\kappa(r)$ is the optical diffusion coefficient defined by

$$\kappa(r) = \frac{1}{3[\mu_a(r)+\mu'_s(r)]} \quad (2)$$

with μ_a and μ'_s representing the absorption coefficient and the reduced scattering coefficient, respectively. The air-tissue boundary is represented by the refractive index mismatch Robin (also known as Type-III) boundary condition, described as⁴⁷

$$-2\alpha\hat{n} \cdot \kappa(r)\nabla\Phi(r) = \Phi(r), \quad (3)$$

where \hat{n} is the unit normal vector on the boundary surface. In Eq. (3), α depends upon the relative refractive index mismatch between the air and tissue interface and is determined by fitting the measurement data with the numerical calculations from the forward model.

2.2.2 Reconstruction algorithm

The objective function (Ω), which minimizes the difference between modeled data (obtained from forward model) and the measurements, if we only reconstruct the absorption coefficient, can be written as⁴⁸

$$\Omega = \min_{\mu_a} \{ \|y - F(\mu_a)\|_2^2 + \lambda \|L(\mu_a - \mu_{a0})\|_2^2 \}, \quad (4)$$

where λ is the regularization parameter and L is a dimensionless penalty matrix which can be obtained from other structural imaging modalities such as CT. When the structural information is not available, the L matrix can be replaced with an identity matrix I . The updating equation based on the Newton iterative method can be written as^{25,49,50}

$$(J^T J + \lambda L^T L) \delta \mu_a = J^T (y - F(\mu_a)), \quad (5)$$

where J represents the Jacobian (sensitivity) matrix with a dimension $[N * M] \times [N * N]$, where $*$ denotes multiplying, M represents the number of measurements, and N is the number of nodes. The update is represented by $\delta \mu_a = \mu_a - \mu_{a0}$. In general, the initial value μ_{a0} is obtained from data fitting procedure⁵¹. The L matrix is calculated before the reconstruction. This type of inclusion of priori information is often referred as soft-priors.^{35,52}

2.3 Mapping of measurement data

Correctly mapping of photon intensity information from an EMCCD camera image to detector nodes on a finite element mesh is critical for the DOT reconstruction. To improve mapping accuracy, we made a reference cylinder which had 24×9 checkerboard on its surface. Each checkerboard was a square with a width of 10.21 mm that was equal to $1/24$ of the cylinder circumference. The 3D physical coordinates of corners for each square were known on the cylinder surface. To map correctly, we took one image of the reference cylinder with our prototype system. There were 6×4 checks in the side field of view. We found pixel coordinates of all 35 corners for squares on the EMCCD camera image manually. Then, using those pixel coordinates and their corresponding physical coordinates, we generated linear mapping matrix

for mapping finite element nodes' coordinates to the corresponding EMCCD camera image pixels. Fig. 2 shows the mapping results using the linear matrix we generated. Ideally, if the mapping was perfect, each red dot in Fig. 2 should be on the crossing points on the checkerboard exactly. Most of the nodes inside the FOV were matched very well, although the nodes far away from the center were not mapped well with the corners of squares because we used a simple linear mapping method and the surface of the cylinder was not flat. The linear mapping matrix is good enough to be used in the phantom experiments because the measurement nodes were not far away from the center.

2.4 Measurement setup

In our DOT prototype system, the EMCCD camera was used as a detector, which could only measure half of the phantom surface in a transmission measurement mode. For each angular projection, the linear stage moved the laser beam 6 steps in the vertical direction with a step size of 5 mm. This system generated 6 laser illumination points on the phantom of interest for each angular projection. For each illumination position, we used all finite element nodes inside a 6 cm wide and 4 cm high measurement patch on the other side of the phantom (Fig. 3b). The numerical simulations reported later have helped us to select the width of the measurement patch.

2.5 Phantom recipe and geometry

A cylindrical phantom with a diameter of 78 mm and a height of 60 mm was made of agar, titanium dioxide (TiO_2), Indian ink, and water. A jelly like soft base phantom was made with a through hole at the target location, which was 15 mm away from the central line of the cylinder. Then, a cylindrical target with a diameter of 10 mm and a height of 10 mm was inserted into the hole on the background phantom. Other sections of the hole were filled with same material as base

phantom (Fig. 3a). The phantom base was fabricated to have $\mu_a = 0.005 \text{ mm}^{-1}$ and $\mu'_s = 1.0 \text{ mm}^{-1}$ at the wavelength of 650 nm. The target had an absorption coefficient of 0.02 mm^{-1} at the wavelength of 650 nm for the 4 times absorption contrast case. The absorption coefficient of the target was 0.01 mm^{-1} for the two times absorption contrast case. For both cases, the reduced scattering coefficient of the target was 1.0 mm^{-1} , the same as the background phantom.

2.6 Measurement data calibration with a homogeneous phantom

We used a cylindrical phantom whose surface was not flat. Different measurement points on the cylindrical surface had different orientations and distances to the EMCCD camera, which resulted in different photon collection coefficients at different pixels. We calibrated our measurements with the same approach described in Ref. 53. At first, we made a homogeneous phantom with the same optical properties and the same geometrical dimensions as the heterogeneous phantom of interest. Secondly, we obtained a set of measurement data D_{ij} at same setup for the heterogeneous phantom. Thirdly, optical properties such as the absorption coefficient μ_a , the reduced scattering coefficient μ'_s and the boundary condition parameter α were determined by data fitting.⁵¹ Then, we calculated the calibration coefficients $f_{ij} = D_{ij}^*/D_{ij}$, where D_{ij}^* are the measurements from forward modeling with the optical properties obtained in the 3rd step. Finally, we multiplied the ratio factor f_{ij} by the measurement data M_{ij} from the heterogeneous phantom to obtain the final calibrated measurements for the DOT reconstruction.

3. RESULTS

3.1 Results of numerical simulations

The measurement projection number and the measurement data volume are important factors for data acquisition time, reconstruction time, and DOT image quality. We conducted a series of

numerical simulations to figure out the optimal number of projections and the width of the EMCCD camera measurement patch. In the numerical simulations, we used a cylindrical phantom with a diameter of 78 mm and a height of 60 mm. A cylindrical target (diameter of 10 mm and height of 20 mm) was placed at 15 mm away from the central line of the phantom. Here we simulated four different data acquisition types: (a) four projections with 3 cm wide measurement patch; (b) four projections with 6 cm wide measurement patch; (c) six projections with 3 cm wide measurement patch; (d) six projections with 6 cm measurement patch. In all cases, the number of source position in each angular projection was 6, and the sources were placed 5 mm apart from each other vertically. The height of detection patch was 4 cm for all cases. We set the reduced scattering coefficient to be 1 mm^{-1} for both the target and the phantom background. The absorption coefficient was 0.007 mm^{-1} for the phantom background and 0.028 mm^{-1} for the target as shown in Table. 1.

For all the four numerical simulation cases (a-d) as described above, 5% Gaussian noise was added to the numerical measurements, which were then used for the iterative DOT reconstruction with L_2 regularization. The absorption coefficient of 0.007 mm^{-1} and the reduced scattering coefficient of 1.0 mm^{-1} were used as the initial guess. The regularization parameter was 0.1 at first and reduced accordingly. A finite element mesh with 9743 nodes, 53030 tetrahedral elements, and 5838 surface elements were used to discretize the virtual phantom and for the forward modeling. The same mesh was also used for the iterative DOT reconstruction. In a cluster with 6 nodes (2.8 GHz each node) and 128 GB memory, each iteration of the DOT reconstruction took 1.52 minutes. The iterative reconstruction ended when the updated values were less than 2%, which took 10 iterations for the numerical simulation with 6 angular projections, 6 cm wide measurement patch, and the virtual CT guidance.

The reconstructed DOT images are plotted in Fig. 4, in which Figs. 4a to 4d are reconstructed for the simulation cases (a) to (d), respectively. Figs. 4a-4b indicate that we cannot reconstruct the target with measurements of 4 angular projections. With measurements of 6 angular projections, the target can be reconstructed, although the reconstructed target sizes and values are not accurate as shown in Fig. 4c for 4 cm wide measurement patch and Fig. 4d for 6 cm wide measurement patch, respectively. Then we repeated the DOT reconstruction with a virtual CT image as the structural prior. The reconstructed images are plotted in Figs. 5a-5d for the numerical simulation cases (a) to (d), respectively. Fig. 5 indicates that we were able to reconstruct good results for all four numerical simulation cases when the virtual CT guidance was applied. The numerical simulation with six angular projections and 6 cm wide measurement patch has the best image quality in terms of the target location and the reconstructed values, as shown in Fig. 5d.

To analyze the reconstructed DOT images quantitatively, we plot the target profiles whose location is indicated by the black dotted line in Fig. 6a. The profiles from Figs. 4 and 5 are plotted in Figs. 6b and 6c, respectively. The profile plots in Fig. 6 further demonstrates that the quality of the reconstructed absorption coefficient images from six angular projections with 6 cm wide measurement patch is the best when the virtual CT image was used as structural prior in the DOT reconstruction. Calculated from the profiles in Fig. 6, the error of the reconstructed absorption coefficient in the target is 1.25% for the numerical simulation case of 6 angular projections, 6 cm wide patch, and with the virtual CT guidance.

3.2 Results of phantom experiments

We evaluated our single wavelength, EMCCD camera based prototype DOT imaging system by performing two set of phantom experiments. The phantom recipe and geometry are described in the method section. The first phantom experiment had 4:1 absorption contrast and the second had

2:1 absorption contrast. The optical properties and geometrical dimensions are given in Table. 2. For each illumination position, we used all finite element surface nodes in a 6 cm wide and 4 cm high patch on the other side of the phantom as detector nodes. The number of nodes inside the patch for each projection was slightly different, and the total number of measurements were 14520 for all projections. We compared reconstruction results among 4 different cases: (a) uncalibrated measurement data without structural guidance; (b) calibrated data without structural guidance; (c) uncalibrated data with structural guidance; and (d) calibrated data with structural guidance. For cases (b) and (d), we calibrated measurement with the method described in section 2.6. For cases (c) and (d), we used the physical location information of the target as the virtual structural prior because the CT scanner was not available during the experimental time. For the phantom experiments, we used the same finite element mesh and the same iterative DOT reconstruction stopping criteria as those in the numerical simulations.

The reconstructed DOT images of the 4:1 absorption contrast phantom are plotted in Fig. 7, in which the ground truth image is plotted in Fig. 7a where the black dotted line cross the target indicates the profile position. There are many artifacts at the boundary in the reconstructed absorption coefficient image using uncalibrated data without structural guidance (as shown in Fig. 7b). Calibration with the homogeneous phantom improves reconstruction results even without structural prior. However, there are still some artifacts at the boundary and the reconstructed absorption coefficient of the target is less than the true value (as shown in Fig. 7c). Reconstruction with the structural guidance using the uncalibrated measurement data outperformed the previous two cases with some artifacts at boundary (as shown in Fig. 7d). And the recovered absorption coefficient of the target is much less than the exact value (as shown in Fig. 7d). Reconstruction

with the structural prior using the calibrated measurements has the best image quality in terms of both target location and the reconstructed absorption coefficients (as shown in Fig. 7e).

The reconstructed DOT images for the 2:1 absorption contrast phantom experiment are plotted in Fig. 8, in which the ground truth image is plotted in Fig. 8a. We observed the same trend as in the 4 times absorption contrast case. Measurement calibration and virtual structural guidance improve the reconstruction results. The reconstructed image using the uncalibrated data without the structural guidance has the worst quality as shown in Fig. 8b. For the reconstruction with the calibrated measurement data and without the structural prior, the reconstructed target is at the right location but there are significant artifacts in the boundary as shown in Fig. 8c. These artifacts are from the measurement noises that deteriorated the reconstruct image quality without the structural guidance. When the structural guidance was applied and the uncalibrated measurement data were used, the reconstructed DOT image is plotted in Fig. 8d, from which we see that the image quality becomes better but there are still some artifacts in the boundary. This indicates that the measurement data need to be calibrated. With the structural prior using calibrated measurements, the target has been reconstructed at the right locations and with correct absorption coefficient as shown in Fig. 8e.

To analyze the reconstructed images quantitatively, we plot the profiles along the position indicated by the black dotted line in Figs. 7a and 8a. The profile plots in Fig. 9 demonstrates that the quality of the reconstructed DOT image from the calibrated data and with a virtual CT guidance has been improved substantially. For the 4 times absorption case, the error of the reconstructed absorption coefficient of the target for the calibrated data with the virtual CT guidance is 2%. The error is 4% for the 2 times absorption contrast case. The target size errors are 9% for both 4 and 2 times absorption contrast cases.

4. DISCUSSION AND FUTURE WORK

We have built the prototype DOT imaging system that mimics our future CT guided DOT imaging system by using the same EMCCD camera and the same collimated laser beam. With both numerical simulations and phantom experiments, we have studied the effects of the projection number and the width of FOV on the reconstructed DOT images. Although we used the virtual CT guidance in the studies, the feasibility study in this paper lays a solid path for our future CT guided DOT imaging system.

The major purpose of the proposed CT guided DOT imaging system is to monitor the breast cancer response to the chemotherapy. Neoadjuvant chemotherapy is widely used in the treatment of locally advanced breast cancer. Monitoring the response to the chemotherapy can improve survival and reduce morbidity. Tumor responsive to the chemotherapy has vascular changes that can be monitored by DOT noninvasively. The total hemoglobin concentration reduction is a major sign for the responsive breast tumors.⁵⁴⁻⁵⁶ Photon scattering in DOT makes it difficult to localize tumor size and position. CT can provide guidance in DOT reconstruction algorithms to minimize the effects of optical scattering for accurately monitoring of breast cancer's response to the chemotherapy.

The major challenge for the CT guided DOT imaging system is that CT does not have very good soft tissue contrast to differentiate tumor very well from its background. Patients with neoadjuvant chemotherapy usually have late stage breast cancers. The CT contrast agents could enhance the breast cancer imaging of CT. Furthermore, the soft prior guidance algorithm can correct the mismatched guidance to some extent (up to 7%) as reported in reference 27.

The homogeneous phantom based calibration method as described in section 2.6 works well for phantom experiments. This method can be applied to *in vivo* breast imaging by scanning a

homogeneous phantom with the same geometry and similar optical properties of the imaged breast. We can obtain the imaged breast geometry from the CT images and then print a mold with a 3D printer. The optical properties can be estimated by the fitting algorithm as described in reference 53. Another approach, one of our future research topics, is to use a ray tracing software (LightTools, Synopsys Inc.) to calculate the photon collection efficiency at different detector positions on the breast surface.

One possible limitation of the proposed CT guided DOT imaging system is the small dynamic range of the EMCCD camera. Another possible limitation is the reflected optical photons from the scanner's rotary gantry to the EMCCD camera. One way to overcome this limitation is to paint black all the components inside the system gantry.

We have investigated the feasibility study of the CT guided DOT imaging with 2 times and 4 times absorption contrast targets for both numerical simulations and phantom experiments. Although these studies can prove the feasibility, we need to include the scattering effects in the future studies, especially when we will include four lasers at four different wavelengths in the future system.

In the future, we will build a multispectral EMCCD camera based DOT imaging system which consists of 4 diode CW lasers, an optical switch, a fiber holder, collimators, an EMCCD camera and a rotation stage. Four CW lasers at wavelengths of 650, 715, 880, and 915 nm are connected to a 4-to-12 optical switch which passes one laser to one of 12 fibers and the laser beam is collimated at the other end of the fiber with a collimator. Measurements at six projections with rotational increments of 60 degrees are taken to cover the whole surface of the breast. Altogether, there are 4 lasers with total 72 excitation positions for each wavelength. For each laser excitation position, pictures are taken by the EMCCD camera as measurements in a transmission mode. The

EMCCD camera based DOT imaging system is integrated into a breast CT imaging system.³⁷ The breast CT imaging system has a powerful rotation gantry, on which optical fiber holder and EMCCD camera are mounted. The schematic of the proposed CT guided DOT imaging system is plotted in Fig. 10. We have selected an optical switch from Dicon Fiberoptics. The switch time is about 0.5 seconds. The rotation time per 60 degrees is estimated to be 5 seconds. The exposure time per measurement picture is estimated to be 1 second per wavelength per position. So that the total measurement time for the DOT imaging is estimated about 8 minutes.

5. CONCLUSION:

In this paper, we proposed a novel CT guided DOT system for breast cancer imaging, which uses an EMCCD camera as a detector without any coupling liquid. We evaluated our prototype system with a set of numerical simulations and phantom experiments. From numerical simulations, we confirmed that the measurement data from six projections with 6 cm wide measurement patch are enough to reconstruct good absorption image with high quantitative accuracy if CT guidance is applied. The phantom experiments further demonstrate that our proposed CT guided DOT system is able to reconstruct 2 times absorption contrast targets at very high spatial resolution and quantitative accuracy. In the future, we will combine our prototype DOT system with a dedicated breast CT system and evaluate the system performance with phantom experiments and patient data.

ACKNOWLEDGMENTS

Authors thank research support from California Breast Cancer Research Program (IDEA: 20IB-0125), the startup fund from UC Merced, and the summer fellowship from the graduate program of Biological Engineering and Small Technologies (BEST), School of Engineering, UC

Merced.

REFERENCES

- [1] A. Jemal, *et al.*, “Cancer statistics, 2016,” *CA: A Cancer Journal for Clinicians* **66**(1), 7–30 (2016) [[doi: 10.3322/caac.21332](https://doi.org/10.3322/caac.21332)].
- [2] L. Tabar, *et al.*, “Mammography service screening and mortality in breast cancer patients: 20-year follow-up before and after introduction of screening,” *The Lancet* **361**(9367), 1405-1410 (2003) [[doi:10.1016/S0140-6736\(03\)13143-1](https://doi.org/10.1016/S0140-6736(03)13143-1)].
- [3] M. C. Segel, D. D. Paulus, and G. Hortobagyi, “Advanced primary breast cancer: assessment at mammography of response to induction chemotherapy,” *Radiology* **169**(1), 49–54 (1988) [[doi:10.1148/radiology.169.1.3420282](https://doi.org/10.1148/radiology.169.1.3420282)].
- [4] V. A. Loving, W. B. DeMartini, P. R. Eby, R. L. Gutierrez, S. Peacock, and C. D. Lehman, “Targeted Ultrasound in women younger than 30 years with focal breast signs or symptoms: outcomes analyses and management implications,” *American Journal of Roentgenology* **195**(6), 1472–1477 (2010) [[doi:10.2214/AJR.10.4396](https://doi.org/10.2214/AJR.10.4396)].
- [5] D. Saslow *et al.*, “American cancer society guidelines for breast screening with MRI as an adjunct to mammography,” *CA: a cancer journal for clinicians* **57**(2), 75–89 (2007) [[doi:10.3322/canjclin.57.2.75](https://doi.org/10.3322/canjclin.57.2.75)].
- [6] R. Gilles *et al.*, “Locally advanced breast cancer: contrast-enhanced subtraction MR imaging of response to preoperative chemotherapy,” *Radiology* **191**(3), 633–638 (1994) [[doi:10.1148/radiology.191.3.8184039](https://doi.org/10.1148/radiology.191.3.8184039)].
- [7] P. J. Drew *et al.*, “Evaluation of response to neoadjuvant chemoradiotherapy for locally advanced breast cancer with dynamic contrast-enhanced MRI of the breast,” *European Journal of Surgical Oncology* **27**(7), 617–620 (2001) [[doi:10.1053/ejso.2001.1194](https://doi.org/10.1053/ejso.2001.1194)].
- [8] C. Balu-Maestro *et al.*, “Imaging in evaluation of response to neoadjuvant breast cancer treatment benefits of MRI,” *Breast cancer research and treatment* **72**(2), 145–152 (2002)

[\[doi:10.1023/A:1014856713942\]](https://doi.org/10.1023/A:1014856713942).

- [9] B. W. Pogue *et al.*, “Characterization of hemoglobin, water, and NIR scattering in breast tissue: analysis of intersubject variability and menstrual cycle changes,” *Journal of biomedical optics* **9**(3), 541–552 (2004) [[doi:10.1117/1.1691028](https://doi.org/10.1117/1.1691028)].
- [10] A. Corlu *et al.*, “Uniqueness and wavelength optimization in continuous-wave multispectral diffuse optical tomography,” *Optics Letters* **28**(23), 2339–2341 (2003) [[doi: 10.1364/OL.28.002339](https://doi.org/10.1364/OL.28.002339)].
- [11] C. Li *et al.*, “Multispectral breast imaging using a ten-wavelength, 64× 64 source/detector channels silicon photodiode-based diffuse optical tomography system,” *Medical physics* **33**(3), 627–636 (2006) [[doi:10.1118/1.2171508](https://doi.org/10.1118/1.2171508)].
- [12] C. Li *et al.*, “Multispectral diffuse optical tomography with absorption and scattering spectral constraints,” *Applied Optics* **46**(34), 8229–8236 (2007) [[doi: 10.1364/AO.46.008229](https://doi.org/10.1364/AO.46.008229)].
- [13] T. O. McBride *et al.*, “Spectroscopic diffuse optical tomography for the quantitative assessment of hemoglobin concentration and oxygen saturation in breast tissue,” *Applied optics* **38**(25), 5480–5490 (1999) [[doi:10.1364/AO.38.005480](https://doi.org/10.1364/AO.38.005480)].
- [14] S. Srinivasan *et al.*, “Spectrally constrained chromophore and scattering near-infrared tomography provides quantitative and robust reconstruction,” *Applied Optics* **44**(10), 1858-1869 (2005) [[doi:10.1364/AO.44.001858](https://doi.org/10.1364/AO.44.001858)].
- [15] Y. Pei, H. Graber, and R. Barbour, “Normalized-constraint algorithm for minimizing inter-parameter crosstalk in DC optical tomography,” *Optics Express* **9**(2), 97–109 (2001) [[doi:10.1364/OE.9.000097](https://doi.org/10.1364/OE.9.000097)].
- [16] B. W. Pogue *et al.*, “Instrumentation and design of a frequency-domain diffuse optical tomography imager for breast cancer detection,” *Optics express* **1**(13), 391–403 (1997) [[doi:10.1364/OE.1.000391](https://doi.org/10.1364/OE.1.000391)].
- [17] B. J. Tromberg *et al.*, “Non-invasive measurements of breast tissue optical properties using

- frequency-domain photon migration,” *Philosophical Transactions of the Royal Society B: Biological Sciences* **352**(1354), 661–668 (1997) [[doi:10.1098/rstb.1997.0047](https://doi.org/10.1098/rstb.1997.0047)].
- [18] Q. Zhu *et al.*, “Utilizing optical tomography with ultrasound localization to image heterogeneous hemoglobin distribution in large breast cancers,” *Neoplasia* **7**(3), 263 (2005) [[doi:10.1593/neo.04526](https://doi.org/10.1593/neo.04526)].
- [19] H. Jiang *et al.*, “Near-infrared optical imaging of the breast with model-based reconstruction,” *Academic radiology* **9**(2), 186-194 (2002) [[doi:10.1016/S1076-6332\(03\)80169-1](https://doi.org/10.1016/S1076-6332(03)80169-1)].
- [20] C. H. Schmitz *et al.*, “Instrumentation for fast functional optical tomography,” *Review of Scientific Instruments* **73**(2), 429–439 (2002) [[doi:10.1063/1.1427768](https://doi.org/10.1063/1.1427768)].
- [21] S. M. Van de Ven *et al.*, “Diffuse optical tomography of the breast: preliminary findings of a new prototype and comparison with magnetic resonance imaging,” *European radiology* **19**(5), 1108–1113 (2009) [[doi:10.1007/s00330-008-1268-3](https://doi.org/10.1007/s00330-008-1268-3)].
- [22] S. B. Colak *et al.*, “Clinical optical tomography and NIR spectroscopy for breast cancer detection,” *IEEE Journal of Selected Topics in Quantum Electronics* **5**(4), 1143–1158 (1999) [[doi:10.1109/2944.796341](https://doi.org/10.1109/2944.796341)].
- [23] J. P. Culver *et al.*, “Three-dimensional diffuse optical tomography in the parallel plane transmission geometry: Evaluation of a hybrid frequency domain/continuous wave clinical system for breast imaging,” *Medical physics* **30**(2), 235-247 (2003) [[doi:10.1118/1.1534109](https://doi.org/10.1118/1.1534109)].
- [24] G. M. Turner *et al.*, “Complete-angle projection diffuse optical tomography by use of early photons,” *Optics Letters* **30**(4), 409–411 (2005) [[doi: 10.1364/OL.30.000409](https://doi.org/10.1364/OL.30.000409)].
- [25] P. K. Yalavarthy *et al.*, “Weight-matrix structured regularization provides optimal generalized least-squares estimate in diffuse optical tomography,” *Medical physics* **34**(6), 2085–2098 (2007) [[doi:10.1118/1.2733803](https://doi.org/10.1118/1.2733803)].
- [26] X. Intes *et al.*, “Diffuse optical tomography with physiological and spatial a priori constraints,” *Physics in medicine and biology* **49**(12), N155-N163 (2004).

- [27] P. K. Yalavarthy *et al.*, “Structural information within regularization matrices improves near infrared diffuse optical tomography,” *Optics Express* **15**(13), 8043–8058 (2007) [[doi: 10.1364/OE.15.008043](https://doi.org/10.1364/OE.15.008043)].
- [28] G. Boverman *et al.*, “Quantitative spectroscopic diffuse optical tomography of the breast guided by imperfect a priori structural information,” *Physics in medicine and biology* **50**(17), 3941–3956 (2005).
- [29] A. Li *et al.*, “Optimal linear inverse solution with multiple priors in diffuse optical tomography,” *Applied Optics* **44**(10), 1948–1956 (2005) [[doi:10.1364/AO.44.001948](https://doi.org/10.1364/AO.44.001948)].
- [30] B. W. Pogue *et al.*, “Implicit and explicit prior information in near-infrared spectral imaging: accuracy, quantification and diagnostic value,” *Philosophical Transactions of the Royal Society of London A: Mathematical, Physical and Engineering Sciences* **369**(1955), 4531–4557 (2011) [[doi:10.1098/rsta.2011.0228](https://doi.org/10.1098/rsta.2011.0228)].
- [31] Q. Fang *et al.*, “Combined optical and X-ray Tomosynthesis breast imaging,” *Radiology* **258**(1), 89–97 (2011) [[doi:10.1148/radiol.10082176](https://doi.org/10.1148/radiol.10082176)].
- [32] Q. Fang *et al.*, “Combined optical imaging and mammography of the healthy breast: optical contrast derived from breast structure and compression,” *IEEE Transactions on Medical Imaging* **28**(1), 30–42 (2009) [[doi:10.1109/TMI.2008.925082](https://doi.org/10.1109/TMI.2008.925082)].
- [33] V. Ntziachristos *et al.*, “MRI-guided diffuse optical spectroscopy of malignant and benign breast lesions,” *Neoplasia* **4**(4), 347–354 (2002) [[doi:10.1038/sj.neo.7900244](https://doi.org/10.1038/sj.neo.7900244)].
- [34] B. A. Brooksby *et al.*, “Near-infrared (NIR) tomography breast image reconstruction with a priori structural information from MRI: algorithm development for reconstructing heterogeneities,” *IEEE Journal of Selected Topics in Quantum Electronics* **9**(2), 199–209 (2003) [[doi:10.1109/JSTQE.2003.813304](https://doi.org/10.1109/JSTQE.2003.813304)].
- [35] B. Brooksby *et al.*, “Imaging breast adipose and fibroglandular tissue molecular signatures by using hybrid MRI-guided near-infrared spectral tomography,” *Proceedings of the National*

- Academy of Sciences* **103**(23), 8828–8833 (2006) [[doi:10.1073/pnas.0509636103](https://doi.org/10.1073/pnas.0509636103)].
- [36] Q. Zhu *et al.*, “Ultrasound-guided optical tomographic imaging of malignant and benign breast lesions: initial clinical results of 19 cases,” *Neoplasia* **5**(5), 379–388 (2003) [[doi:10.1016/S1476-5586\(03\)80040-4](https://doi.org/10.1016/S1476-5586(03)80040-4)].
- [37] J. M. Boone *et al.*, “Computed tomography for imaging the breast,” *Journal of mammary gland biology and neoplasia* **11**(2), 103–111 (2006). [[doi:10.1007/s10911-006-9017-1](https://doi.org/10.1007/s10911-006-9017-1)]
- [38] K. Yang *et al.*, “A geometric calibration method for cone beam CT systems,” *Medical physics* **33**(6), 1695–1706 (2006) [[doi:10.1118/1.2198187](https://doi.org/10.1118/1.2198187)].
- [39] L. V. Wang and H. Wu, *Biomedical optics: principles and imaging*, John Wiley & Sons, Hoboken, New Jersey (2012) [[doi: 10.1002/9780470177013](https://doi.org/10.1002/9780470177013)].
- [40] A. Ishimaru, *Wave propagation and scattering in random media*, vol. 2, Academic press, New York (1978).
- [41] S. R. Arridge, “Optical tomography in medical imaging,” *Inverse problems* **15**(2), R41-R93 (1999).
- [42] S. R. Arridge and J. C. Schotland, “Optical tomography: forward and inverse problems,” *Inverse Problems* **25**(12), 123010 (2009).
- [43] S. R. Arridge and J. C. Hebden, “Optical imaging in medicine: II. Modelling and reconstruction,” *Physics in Medicine and Biology* **42**(5), 841-853 (1997).
- [44] A. Gibson, J. Hebden, and S. R. Arridge, “Recent advances in diffuse optical imaging,” *Physics in Medicine and Biology* **50**(4), R1-R43 (2005).
- [45] T. Durduran *et al.*, “Diffuse optics for tissue monitoring and tomography,” *Reports on Progress in Physics* **73**(7), 076701 (2010).
- [46] K. D. Paulsen and H. Jiang, “Spatially varying optical property reconstruction using a finite element diffusion equation approximation,” *Medical Physics* **22**(6), 691–701 (1995) [[doi:10.1118/1.597488](https://doi.org/10.1118/1.597488)].

- [47] H. Dehghani et al., “Near infrared optical tomography using NIRFAST: Algorithm for numerical model and image reconstruction,” *Communications in numerical methods in engineering* **25**(6), 711–732 (2009) [[doi: 10.1002/cnm.1162](https://doi.org/10.1002/cnm.1162)].
- [48] A. N. Tikhonov, “Regularization of incorrectly posed problems,” in *SOVIET MATHEMATICS DOKLADY*, **4**(6), 1624-1627 (1963).
- [49] A. Franchois and C. Pichot, “Microwave imaging-complex permittivity reconstruction with a Levenberg-Marquardt method,” *IEEE Transactions on Antennas and Propagation* **45**(2), 203-215 (1997) [[doi:10.1109/8.560338](https://doi.org/10.1109/8.560338)].
- [50] H. Jiang et al., “Simultaneous reconstruction of optical absorption and scattering maps in turbid media from near-infrared frequency-domain data,” *Optics Letters* **20**(20), 2128–2130 (1995) [[doi: 10.1364/OL.20.002128](https://doi.org/10.1364/OL.20.002128)].
- [51] B. W. Pogue et al., “Calibration of near-infrared frequency-domain tissue spectroscopy for absolute absorption coefficient quantitation in neonatal head-simulating phantoms,” *Journal of Biomedical Optics* **5**(2), 185–193 (2000) [[doi:10.1117/1.429985](https://doi.org/10.1117/1.429985)].
- [52] B. Brooksby et al., “Combining near-infrared tomography and magnetic resonance imaging to study in vivo breast tissue: implementation of a Laplacian-type regularization to incorporate magnetic resonance structure,” *Journal of Biomedical Optics* **10**(5), 051504 (2005) [[doi:10.1117/1.2098627](https://doi.org/10.1117/1.2098627)].
- [53] C. Li and H. Jiang, “A calibration method in diffuse optical tomography,” *Journal of Optics A: Pure and Applied Optics* **6**(9), 844-852 (2004). [[10.1088/1464-4258/6/9/005](https://doi.org/10.1088/1464-4258/6/9/005)]
- [54] R. Choe et al., “Diffuse optical tomography of breast cancer during neoadjuvant chemotherapy: A case study with comparison to MRI,” *Med. Phys.* **32**(4), 1128-1139 (2005) [[doi:10.1118/1.1869612](https://doi.org/10.1118/1.1869612)]
- [55] S. Jiang S et al., “Evaluation of breast tumor response to neoadjuvant chemotherapy with tomographic diffuse optical spectroscopy: Case studies of tumor region-of-interest changes,”

Radiology. **252**(2), 551-560(2009) [[doi: 10.1148/radiol.2522081202](https://doi.org/10.1148/radiol.2522081202)]

- [56] D.B. Jakubowski DB *et al.*, “Monitoring neoadjuvant chemotherapy in breast cancer using quantitative diffuse optical spectroscopy: A case study,” *J. Biomed. Opt.* **9**(1): 230-238(2004) [[doi:10.1117/1.1629681](https://doi.org/10.1117/1.1629681)]

Tables:

Table 1: Optical properties and geometry dimensions of the phantom for simulations.

	Diameter	Height	μ_a	μ'_s
Background	78.0 mm	60.0 mm	0.007 mm ⁻¹	1.0 mm ⁻¹
Target	10.0 mm	20.0 mm	0.028 mm ⁻¹	1.0 mm ⁻¹

Table 2 Optical properties and geometrical dimensions of the experimental phantoms.

	Diameter	Height	μ_a	μ'_s
Background	78.0 mm	60.0 mm	0.005 mm ⁻¹	1.0 mm ⁻¹
Target (4:1 μ_a contrast)	10.0 mm	10.0 mm	0.02 mm ⁻¹	1.0 mm ⁻¹
Target (2:1 μ_a contrast)	10.0 mm	10.0 mm	0.01 mm ⁻¹	1.0 mm ⁻¹

Figure Captions :

Fig. 1 Photo of the prototype DOT imaging system.

Fig. 2 Mapped reference nodes in an image taken by the EMCCD camera.

Fig. 3 (a) Phantom geometry. (b) Source nodes (black) and detector nodes (red) in a 6 cm wide measurement patch for an angular projection.

Fig. 4 Transverse sections of the reconstructed absorption coefficient images without virtual CT guidance from numerical measurements with 5% Gaussian noise added for cases (a) four angular projections with 3 cm wide measurement patch; (b) four angular projections with 6 cm wide measurement patch; (c) six angular projections with 3 cm wide measurement patch; and (d) six angular projections with 6 cm wide measurement patch. The black circles denote the target locations.

Fig. 5 Transverse sections of the reconstructed absorption coefficient images with virtual CT guidance from simulated measurements with 5% Gaussian noise added for cases (a) four angular projections with 3 cm wide measurement patch; (b) four angular projections with 6 cm wide measurement patch; (c) six angular projections with 3 cm wide measurement patch; and (d) six angular projections with 6 cm wide measurement patch. The black circles denote the target locations.

Fig. 6 Profile plots of the reconstructed absorption coefficient images cross the target. (a) The black dotted line in the ground truth image indicating the profile position. Profile plots (b) from figure 4 for numerical measurements with 5% Gaussian noise and without the virtual CT guidance; (c) from figure 5 for numerical measurements with 5% Gaussian noise and with the virtual CT guidance.

Fig. 7 Transverse sections of the ground truth image (a) and the reconstructed absorption

coefficient images (b-e) with measurements at six projections for the 4:1 absorption contrast case. The reconstructed absorption image for (b) uncalibrated data without structural guidance; (c) calibrated data without structural guidance; (d) uncalibrated data with structural guidance; and (e) calibrated data with structural guidance. The dotted black line in (a) indicates the profile position. The black circles in (b-e) denote the target locations.

Fig. 8 Transverse sections of the ground truth image (a) and the reconstructed absorption coefficient images (b-e) with measurements at six projections for the 2:1 absorption contrast case. The reconstructed absorption image for (b) uncalibrated data without structural guidance; (c) calibrated data without structural guidance; (d) uncalibrated data with structural guidance; and (e) calibrated data with structural guidance. The dotted black line in (a) indicates the profile position. The black circles in (b-e) denote the target locations.

Fig. 9 Profile plots of the reconstructed absorption coefficient images for (a) 4:1 absorption contrast experiment from Fig. 7 and (b) 2:1 absorption contrast experiment from Fig. 8.

Fig. 10 Schematic of the proposed CT guided DOT imaging system.

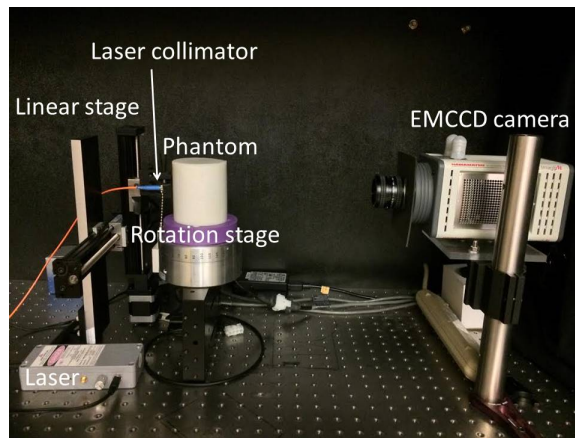


Figure 1

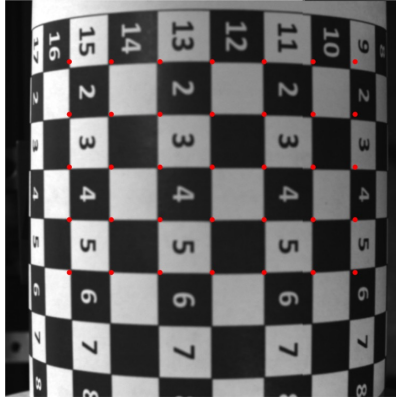


Figure 2

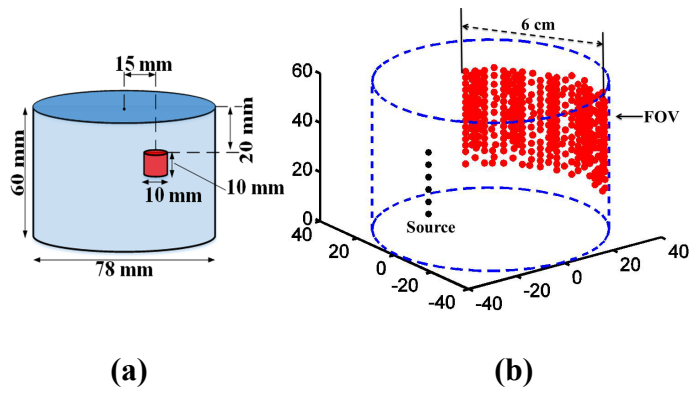


Figure 3

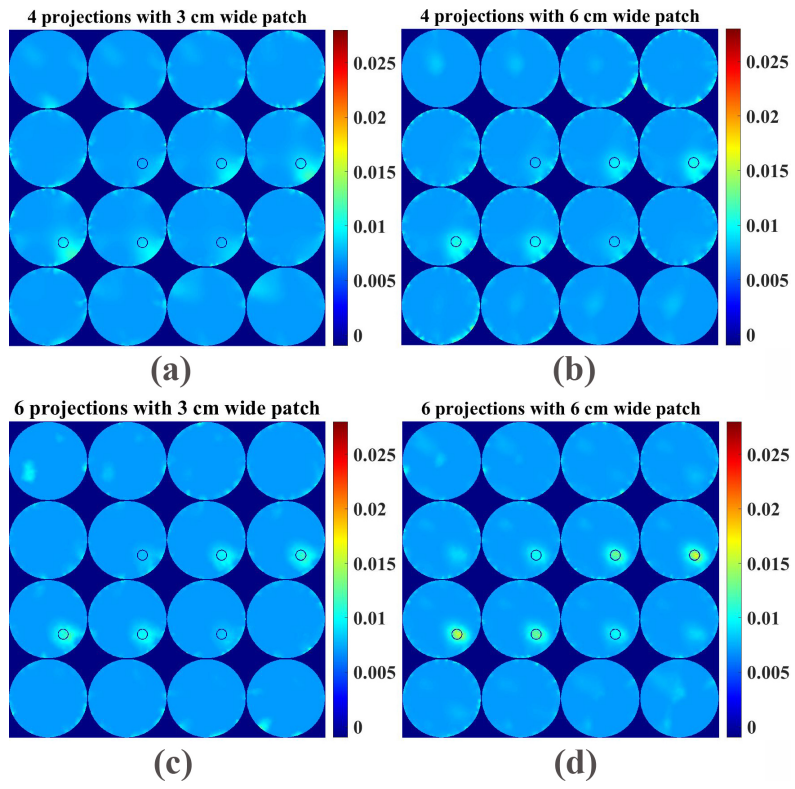


Figure 4

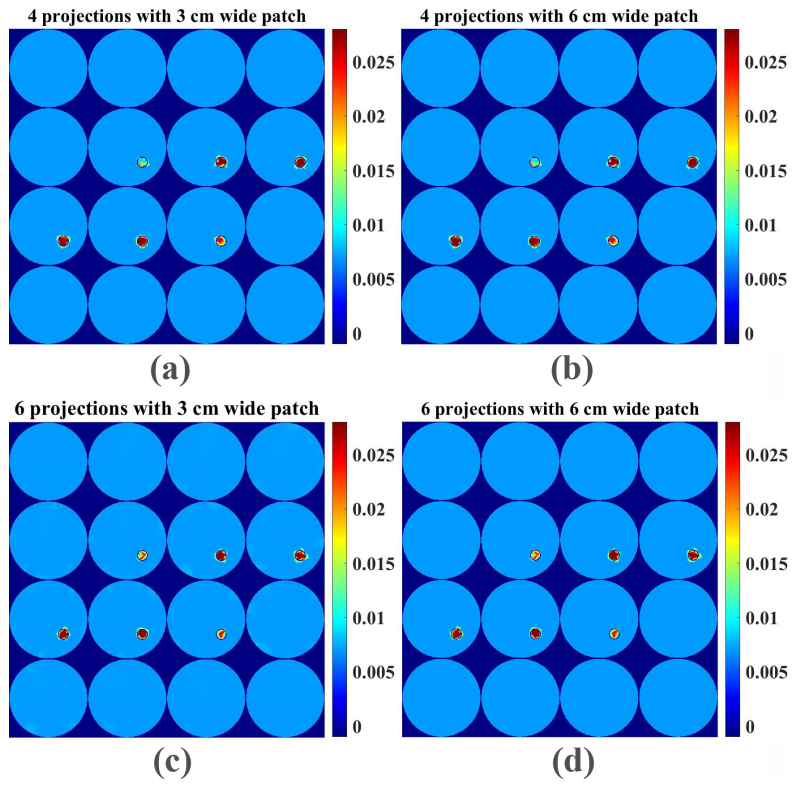
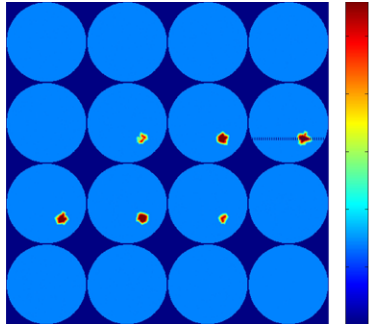
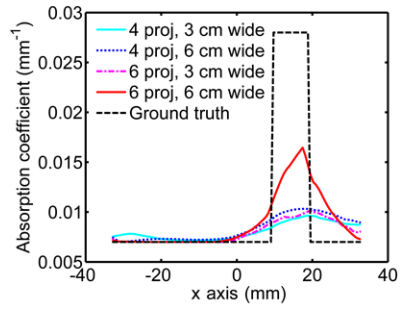


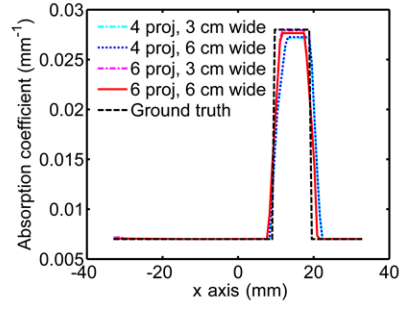
Figure 5



(a)



(b)



(c)

Figure 6

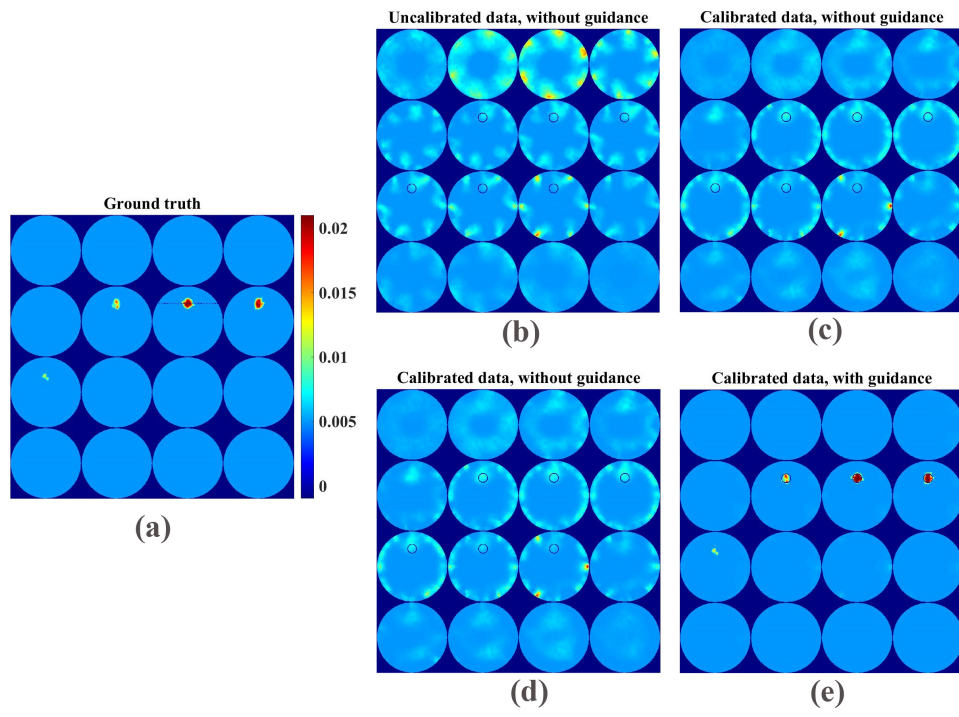


Figure 7

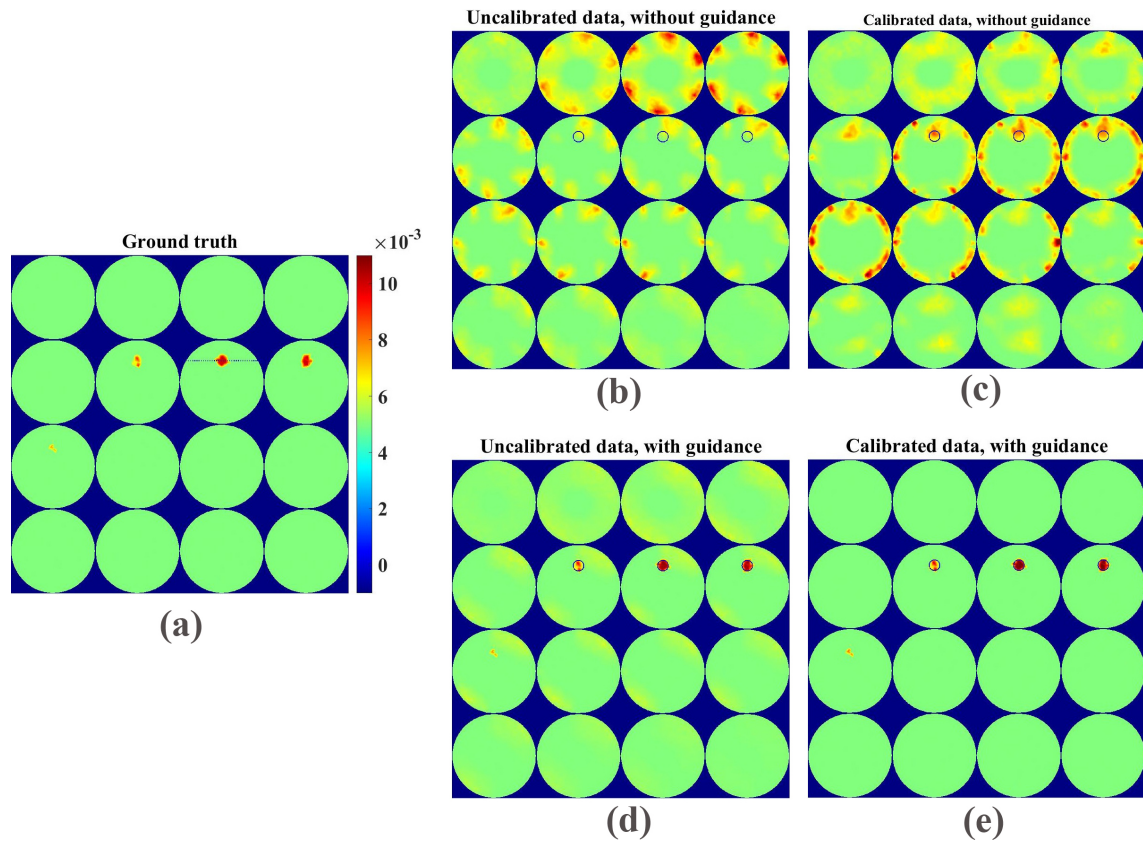


Figure 8

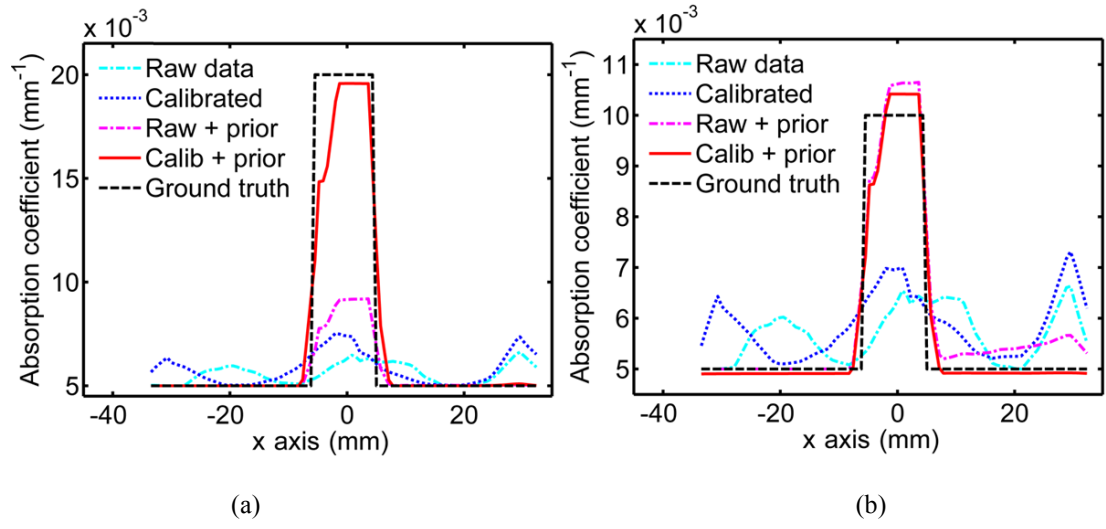


Figure 9

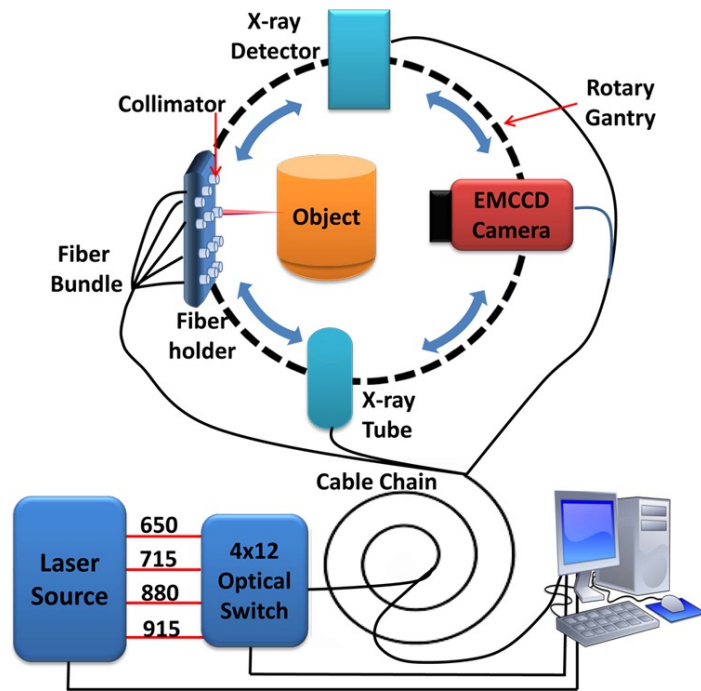


Figure 10